Journal of Materials Chemistry C

ROYAL SOCIETY OF CHEMISTRY

PAPER

Published on 19 October 2026
Licensed under CC-BY-NC 4.0

Check for updates

Cite this: DOI: 10.1039/d6tc02161a

Exploring the design space of SMART RHESINs as a modular nanocapsule platform for functional magnetic nanoparticles

Julia Feye, [abi] David Rudolph, [b] Jens Treptow, [b] Eileen List, [c] Luan Passini, [d] Aritz Lafuente, [e] Frank Mickoleit, [f] Sophia Tessaro, [f] Andreas Maurer, [gh] Serhat Ilbey, [i] Jochen Franke, [i] René Uebe, [f] Dirk Schüler, [f] Alejandro G. Roca, [e] Clément Roux, [d] Hans-Achim Wagenknecht, [c] Claus Feldmann, [b] Peter W. Roesky [b] and Esther S. Rösch *[a]

Magnetic core/shell nanoparticles (CSNPs) are central to emerging imaging and theranostic concepts, yet translating different magnetic payloads into a common, chemically addressable and functionally expandable architecture remains challenging. SMART RHESIN nanocapsules encapsulate different magnetic nanoparticle (NP) systems within a protective phenolic resin shell and permit structural variation and post-synthetic functionalisation. Here we map the design space of SMART RHESIN phenolic resin hollow nanocapsules across 52 reactions varying monomer choice, CSNP type, loading, co-encapsulation, and polymer additives. The platform incorporates magnetic payloads ranging from lab-synthesised magnetite to commercial iron oxides and cubic NPs, while identifying biogenic magnetosomes as a boundary case for the present synthesis conditions, with the resulting nanocapsule diameter (about 100 to 400 nm) and shell thickness (about 10 to 80 nm) varying systematically with the choice of CSNP system and reaction conditions. Magnetic particle spectroscopy (MPS) indicates reduced viscosity-induced phase shifts for selected representative formulations from this expanded compositional set, phantom MPI demonstrates multi-colour imaging that resolves aqueous and immobilised SR29 signals within a single field of view, and surface carboxylates enable post-synthetic modification, illustrated by ^{18}F-radiolabelling for PET/CT. These findings establish SMART RHESINs as a versatile nanocapsule platform for integrating magnetic NPs with additional optical, radiochemical and future targeting functionalities.

Received 30th June 2026,
Accepted 11th September 2026

DOI: 10.1039/d6tc02161a

rsc.li/materials-c

[a] Faculty of Engineering, Baden-Württemberg Cooperative State University Karlsruhe, Erzbergerstr. 121, 76133 Karlsruhe, Germany. E-mail: esther.roesch@dhbw-karlsruhe.de
[b] Institute of Inorganic Chemistry, Karlsruhe Institute of Technology, Engesserstraße 15, 76131 Karlsruhe, Germany
[c] Institute of Organic Chemistry, Karlsruhe Institute of Technology, Fritz-Haber-Weg 6, 76131 Karlsruhe, Germany
[d] Laboratoire Softmat, Université de Toulouse, CNRS UMR 5623, Université Toulouse III – Paul Sabatier, 118 Route de Narbonne, 31062 Toulouse, France
[e] Catalan Institute of Nanoscience and Nanotechnology (ICN2), CSIC and BIST, Campus UAB, Bellaterra, 08193 Barcelona, Spain
[f] Department of Microbiology, University of Bayreuth, Universitätsstraße 30, 95447 Bayreuth, Germany
[g] Department of Preclinical Imaging and Radiopharmacy, Werner Siemens Imaging Center, Eberhard Karls University Tübingen, Röntgenweg 15, 72076 Tübingen, Germany
[h] Cluster of Excellence iFIT (EXC 2180) "Image-Guided and Functionally Instructed Tumour Therapies", Eberhard Karls University Tübingen, 72076 Tübingen, Germany
[i] Bruker BioSpin GmbH & Co. KG, Preclinical Imaging Division, Rudolf-Plank-Straße 23, 76275 Ettlingen, Germany

Introduction

Magnetic nanoparticles (NPs) play an important role in modern medical diagnostics[1] where they are used as tracers or contrast agents in applications such as magnetic resonance imaging (MRI)[2] and magnetic particle imaging (MPI).[3,4] Consistent magnetic NP properties are particularly relevant to biomedical applications and the reaction control of the NP synthesis is therefore of great importance for their final properties, as they depend on many factors such as particle size, shape, composition, aggregation, and surface functionalisation.[5,6] Magnetic core/shell nanoparticles (CSNPs) can be synthesised by a variety of chemical approaches (*i.e.* co-precipitation, microemulsions, sol–gel reaction, hydrothermal and thermal decomposition), with different size distributions, shape control, degree of crystallinity and yield.[7–9] In addition, magnetic CSNPs are naturally mineralized by magnetotactic bacteria. A well-studied example is the model organism *Magnetospirillum gryphiswaldense*[10,11] that produces approximately

40 cuboctahedral, membrane-enveloped magnetite CSNPs, so-called magnetosomes, through a genetically controlled biomineralisation process.[12,13]

Our group previously introduced SMART RHESINs as hollow nanocapsules for the encapsulation of a defined CSNP system.[14] While this initial work established the feasibility of CSNP incorporation, the comparatively small magnetic cores provided insufficient magnetisation for MPI applications. We subsequently advanced the concept using the synomag-D-loaded SMART RHESIN variant SR33, demonstrating viscosity-independent MPI reconstruction.[15] However, the broader synthetic scope, structural tunability and functional modularity of the SMART RHESIN platform remained unexplored. Here, we map the design space of SMART RHESINs across 52 reactions in five experimental series, covering CSNPs with different sizes, shapes, surface chemistries and origins, including lab-synthesised, commercial, cubic and biogenic magnetic NPs. We further demonstrate co-encapsulation of magnetic and luminescent payloads, evaluate PEG and PVP as additives that influence nanosphere size and shell thickness in a CSNP-dependent manner, and provide a first *in vivo* PET/CT feasibility assessment using an ^{18}F-labelled, surface-functionalised SMART RHESIN variant. MPI performance remains strongly dependent on tracer properties, as signal strength and spatial resolution are influenced by particle size distribution, temperature, and matrix-related environmental factors such as viscosity which affect Brownian and Néel relaxation.[16] Remmo *et al.* showed that one citrate-coated synomag variant (SynC30) exhibited enhanced magnetic particle spectroscopy (MPS) and MPI signals under immobilised conditions.[17] Building on these findings, the present work extends the SMART RHESIN platform from the single magnetite system originally reported to a broad range of MPI-relevant CSNPs, including high-magnetisation and shape-anisotropic cores, while preserving the encapsulation-mediated decoupling from the surrounding matrix. MPI is a non-invasive, radiation-free imaging modality that detects the non-linear magnetic response of superparamagnetic NPs, which is governed by Brownian and Néel relaxation.[18–20] The signal intensity is proportional to tracer concentration, enabling intrinsic quantification at any tissue depth.[21] Encapsulation of CSNPs within SMART RHESIN nanocapsules stabilizes effective relaxation and renders the MPS signal largely insensitive to viscosity variations, as previously shown for selected systems.[14,15] In the present work, MPS and MPI are therefore used to evaluate representative formulations from the broader SMART RHESIN design space. Magnetic NP relaxation involves both Brownian and Néel mechanisms, with Brownian relaxation being sensitive to environmental viscosity. While embedding NPs in dense polymer matrices can suppress Brownian relaxation, this may compromise applications such as magnetic hyperthermia that depend on Brownian motion.[22,23] In SMART RHESINs, the hollow nanosphere shell provides a protective yet flexible microenvironment that decouples magnetic NP cores from the external milieu, reducing viscosity-induced signal variations without fully inhibiting Brownian relaxation and preserving the complex relaxation behaviour required for robust MPI.[14,15] MPI performance is further influenced by matrix composition and temperature, which differ between *in vitro* and *in vivo* conditions.[16] By stabilizing intrinsic CSNP relaxation dynamics, SMART RHESINs may improve the robustness of MPI tracer responses across analytical, frequency-space and particle model-based reconstruction frameworks.[24,25] For instance, particle size and shape critically influence absorption, distribution, metabolism, and excretion (ADME), as well as pharmacokinetics and biodistribution.[26,27] However, biological behaviour depends not only on the size but also on particle composition, surface properties, and application-specific factors.[28] For example, polymeric CSNPs show slower tumour clearance than silica NPs,[28] particles in the 100–200 nm range are frequently investigated for enhanced permeability and retention (EPR)-based tumour targeting,[29] whereas very small iron oxide CSNPs below 10 nm are rapidly cleared from circulation or renally excreted.[27,28] Vascular cut-off sizes can exceed 400 nm for certain tumour types (*e.g.*, colon carcinoma LS174T, murine fibrosarcoma ST-8, murine mammary carcinoma MCa IV).[30,31] These considerations emphasize the need to tailor SMART RHESIN size and chemistry to the intended application. In this context, hollow nanospheres with effective diameters of approximately 200 nm were targeted with the aim to mitigate the rapid blood clearance and accumulation in liver and spleen commonly observed for systemically administered NPs.[28] To enable such tailoring, a detailed understanding of the reaction conditions is essential. Therefore, this study establishes SMART RHESINs as a versatile nanocapsule platform (Fig. 1) capable of encapsulating a broad range of state-of-the-art CSNPs without additional core modification. Building on the previously reported structural and surface-chemical characterization of the base SMART RHESIN architecture, including STEM/EDXS and shell FTIR analysis,[14] we focus here on expanding and defining the synthetic design space of the platform. This includes the influence of phenolic monomer, CSNP type and surface chemistry, CSNP concentration, micelle-forming additives on capsule formation, morphology, and structural integrity. The presence of surface carboxylic acid groups further enables post-synthetic functionalisation, including luminescence labelling, radiolabelling, or future targeting strategies. Together, these investigations define the accessible design space of SMART

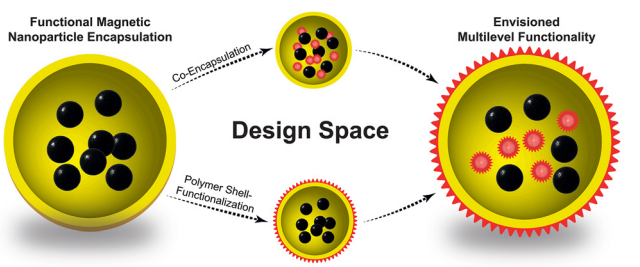


Fig. 1 SMART RHESIN platform design space. Magnetic nanoparticle-filled SMART RHESINs are explored as modular nanocapsules whose functionality can be expanded by co-encapsulation and polymer-shell/surface functionalisation. The right-hand particle depicts an envisioned future architecture combining these independently demonstrated design elements.

This journal is © The Royal Society of Chemistry 2026

RHESINs and provide a basis for future integrated nanocapsules that combine magnetic imaging functionality with additional diagnostic, optical, therapeutic, or targeting modules. Here, the term 'modular' refers to a common phenolic-resin nanocapsule architecture that permits formulation-specific variation of the magnetic payload and the introduction of additional functions through co-encapsulation or post-synthetic surface functionalisation. The extent to which these elements can be combined depends on their compatibility with the synthesis.

Results and discussion

SMART RHESINs were synthesised using mixed P123/sodium oleate (SO) micelles, with or without polymer additives, which encapsulate CSNPs and act as soft-templates for polymer shell formation from phenolic monomers (resorcinol or 2,4-dihydroxybenzoic acid (DHB)) and hexamethylenetetramine (HMT), yielding hollow phenolic formaldehyde resin (PFR) nanospheres (Fig. 2). The synthesis followed established protocols[14,32–34] and resulted in SMART RHESIN nanosphere diameters, d_{SR}, ranging mainly from about 100 to 400 nm, and shell thicknesses, d_{Shell}, of about 10 to 80 nm (determined from scanning transmission electron microscopy (STEM) images) (Fig. 2c).[14] Such structures are commonly referred to as yolk/shell or nanorattle architectures.[35,36] The PFR shell is formed from DHB and HMT, with reactive phenolic derivatives preferred over phenol.[32,37] DHB promotes hollow nanosphere formation[38,39] and introduces surface carboxylic acid groups for further functionalisation.[14,40] These groups could also enable covalent attachment of amine-terminated PEG as a future strategy to improve colloidal stability; however, this approach has not yet been evaluated. Previous studies indicate that carboxylic acid-containing monomers, as seen with DHB and 3-(4-hydroxyphenyl) propionic acid, favour hollow morphologies, whereas purely phenolic monomers such as phenol, resorcinol, and phloroglucinol, yield fully packed structures,[38,39] likely due to altered reaction mechanisms.[39,41] Encapsulation of various CSNPs using micelle-based soft-templating has been reported, including PtCo[42] and iron oxide systems,[32,43] with nanosphere size and shell thickness governed by synthesis conditions.[38,44] However, systematic studies on DHB-based CSNP-filled phenolic formaldehyde resin hollow nanospheres remain scarce. The formation mechanism is complex and influenced by monomer choice, surfactants, temperature, concentrations, crosslinker and core–shell composition. For biomedical translation, nanosphere size and shell properties are critical parameters.[27–31,45–48]

Synthesis of SMART RHESINs

In total, 52 distinct SMART RHESIN reactions were analysed by STEM, revealing a broad distribution of SMART RHESIN diameters and shell thicknesses (Fig. 2c). Two samples (SR38 and SR22) had diameters below 100 nm, 21 samples ranged from 100–199 nm, 14 from 200–299 nm, and 12 samples exceeded 300 nm, while no reliable size could be determined for three samples (SR20, SR49, SR51). These results demonstrate that nanosphere size strongly depends on synthesis conditions and the encapsulated CSNP type. For instance, encapsulation of SPA20-10 NPs (SI 1, Table S1.3) yielded smaller

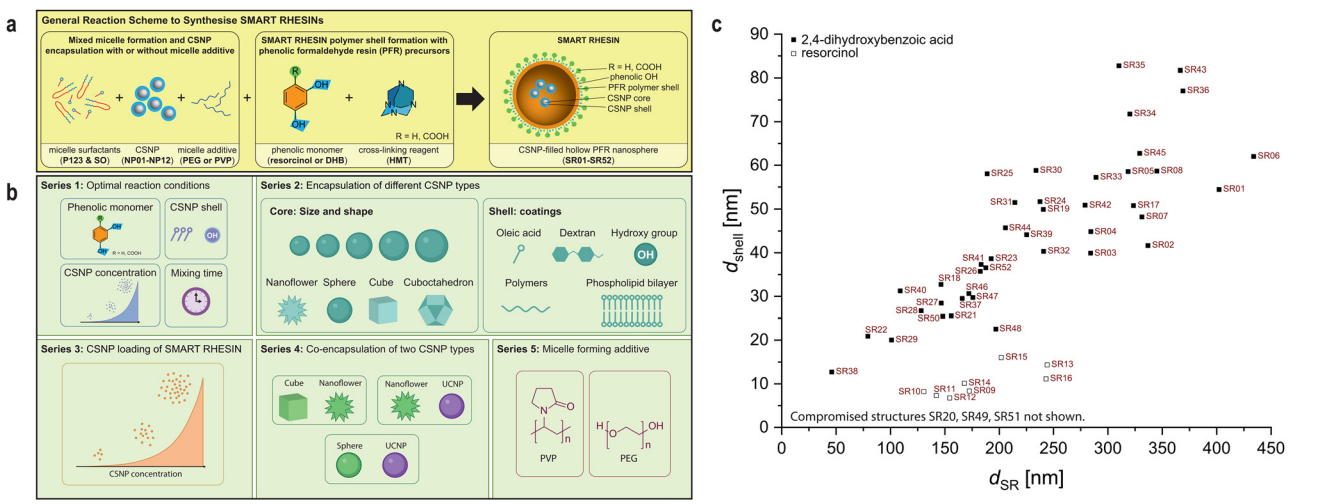


Fig. 2 (a) Illustration of the reaction scheme to synthesise SMART RHESINs. Mixed micelles of P123 and sodium oleate (SO) with or without polymer additive (PEG or PVP) encapsulating CSNPs are used as soft-template for the polymer shell formation with phenolic monomer (resorcinol or DHB) and cross-linking reagent (HMT) to generate hollow PFR nanospheres, named SMART RHESINs. (b) Overview of the conducted reaction series on investigating the impact of reaction parameters on the structural properties of SMART RHESIN hollow nanospheres. Series 1: screening for the optimal reaction conditions varying the phenolic monomer, CSNP shell, CSNP concentration, and micelle forming solution mixing time. Series 2: encapsulation of different CSNP types, *i.e.*, with different sizes, shapes (nanoflower, sphere, cube, cuboctahedron) and shells (oleic acid, dextran, hydroxy group, polymers (PMAO, PEG), and phospholipid bilayer). Series 3: effect of CSNP input concentration on SMART RHESIN morphology and the qualitative CSNP distribution observed by STEM for three different CSNP types (synomag-D, SPA20-10 and cubic CSNP). Series 4: co-encapsulation of two different CSNP types (cubic CSNP with nanoflower, nanoflower with upconverting NP (UCNP), sphere with UCNP). Series 5: use of two concentrations of a polymer additive during micelle formation (PVP and PEG) to adjust size and shell thickness of SMART RHESINs. (c) SMART RHESIN platform—SR-diameter coverage. Mean d_{SR} over mean d_{shell} from STEM particle counts (n = 100) for all 52 reactions (compromised structures SR20, SR49, and SR51 not shown).

SMART RHESINs with an average diameter d_{SR} of around 171 nm, whereas synomag-D (SI 1, Table S1.4) produced significantly larger structures with an average d_{SR} of around 295 nm, highlighting that SMART RHESIN morphology is strongly governed by the encapsulated CSNP system and must therefore be optimised for each NP class. Thus, the SMART RHESIN platform should not be regarded as a single fixed NP formulation, but rather as a tunable design space for adapting magnetic nanocapsules to different physicochemical and biomedical requirements.

To systematically optimize the synthesis of SMART RHESINs and assess the versatility of the platform, five experimental series were performed (SI 1 on Series 1–5). The studies addressed key parameters influencing nanosphere formation, including the phenolic monomer, CSNP surface polarity, CSNP type and concentration, co-encapsulation of different NP types, and the use of polymer additives during micelle formation (SI 2 on Reaction conditions). The resulting SMART RHESINs were evaluated mainly by dynamic light scattering (DLS) and (S)TEM (SI 3 on Particle size) with respect to particle diameter, shell thickness, and structural integrity (SI 4 on STEM). Together, these experiments established suitable synthesis conditions and identified critical factors governing successful encapsulation and structural control.

Series 1 was designed to identify suitable reaction conditions for SMART RHESIN formation by systematically varying the phenolic monomer, CSNP surface polarity, magnetite concentration, and micelle-solution mixing time across SR01–SR16 (SI 1 on Series 1–5, Series 1). The resulting nanospheres were evaluated by DLS and STEM with respect to particle diameter, shell thickness, and qualitative CSNP distribution and apparent loading observed in the STEM images. DHB-based reactions SR01–SR08 yielded hollow SMART RHESIN nanospheres with clearly defined polymer shells, whereas resorcinol-based reactions SR09–SR16 produced smaller, compact particles with only very thin shells. Polar OH-functionalised CSNPs SR01–SR04 and SR09–SR12 showed a more homogeneous CSNP distribution in the STEM images than oleic-acid-coated non-polar CSNPs SR05–SR08 and SR13–SR16, which tended to aggregate and led to polydisperse nanospheres with heterogeneous CSNP distributions. The CSNP concentration affected particle size and the qualitative CSNP distribution observed by STEM in a system-dependent manner, while extending the micelle-solution mixing time from 15 min to 16 h showed no clear benefit. Therefore, DHB, polar CSNPs, and a 15 min mixing time, represented by SR03, were selected as the standard conditions for subsequent syntheses.

Series 2 evaluated the versatility of the optimised SMART RHESIN synthesis conditions by testing the encapsulation of different CSNP types, including lab-synthesised magnetite SR03 and SR07, synomag-D SR17, Ocean NanoTech NPs (SPA20-10, SOR20-10, SMG20-05) SR18–SR20, cubic iron oxide NPs SR21–SR22, and biogenic magnetosomes SR23–SR24 (Fig. 3 and SI 1 on Series 1–5, Series 2). All reactions were performed using DHB and a 15 min micelle-solution mixing time. Most CSNPs, particularly OH-functionalised magnetite SR03, synomag-D SR17,

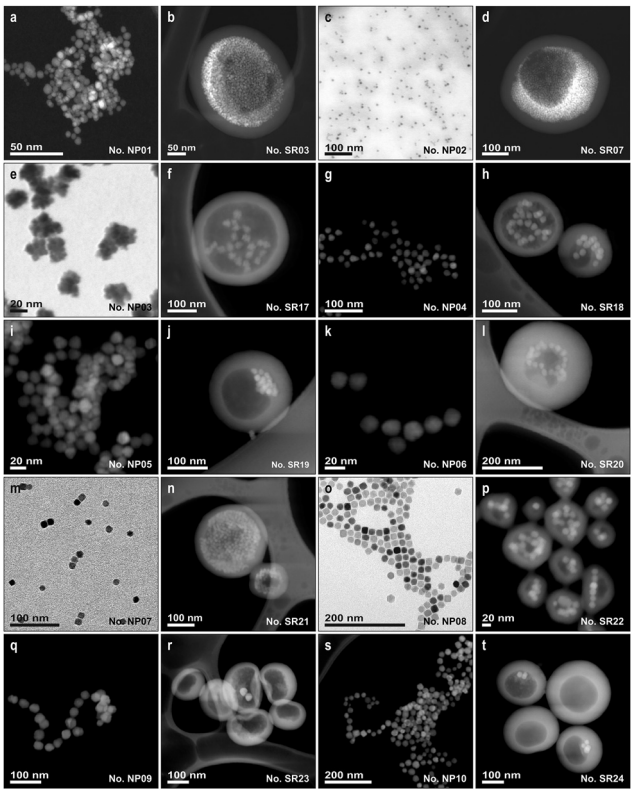


Fig. 3 STEM images of SMART RHESINs with various encapsulated CSNPs (SI 1, Table S1.2). (a) Lab-synthesised polar magnetite encapsulated in (b). (c) Lab-synthesised non-polar magnetite encapsulated in (d). (e) Synomag-D encapsulated in (f). (g) SPA20-10 (PMAO) encapsulated in (h). (i) SOR20-10 (oleic acid) encapsulated in (j). (k) SMG20-05 (PEG) encapsulated in (l). (m) Cubic iron oxide AKB180PM4 encapsulated in (n). (o) Cubic iron oxide AKB121PM4 encapsulated in (p). (q) Wild-type magnetosomes with phospholipid bilayer encapsulated in (r). (s) Δ*feoAB1* magnetosomes (phospholipid bilayer removed and replaced by OH groups) encapsulated in (t). The STEM images c, e, m, and o were acquired in bright field mode, while all other STEM images are shown in dark field mode.

PMAO-coated SPA20-10,[49] and PMAO-coated cubic NPs SR21–SR22, could be successfully encapsulated into hollow SMART RHESIN nanospheres. In contrast, PEG-coated SMG20-05 CSNPs compromised the nanosphere structure (SR20), and magnetosomes SR23–SR24 showed strong aggregation, which prevented efficient encapsulation. Oleic-acid-coated CSNPs SR07 and SR19 could be incorporated, but the resulting nanospheres showed increased polydispersity or heterogeneous CSNP distributions in the STEM images. Overall, Series 2 demonstrates that SMART RHESINs can encapsulate a broad range of CSNPs, provided that aggregation in the aqueous reaction medium is sufficiently controlled.

Series 3 investigated how the CSNP concentration affects SMART RHESIN filling density (as judged by STEM), particle size, and structural integrity under the optimised synthesis conditions using DHB and a 15 min mixing time. Concentration series were performed with SPA20-10 CSNPs SR25–SR29 and SR18 for PMAO-coated particles, SR30 and SR19 for SOR20-10 oleic-acid-coated particles, and SR20 for SMG20-05 PEG-coated particles (SI 1, Fig. S1.3 and Table S1.3), as well as with synomag-D

 This journal is © The Royal Society of Chemistry 2026

SR31–SR36 and SR17 (SI 1, Fig. S1.4 and Table S1.4), and cubic iron oxide CSNPs SR37, SR21, SR22, and SR38 (SI 1, Fig. S1.5 and Table S1.5). SPA20-10 CSNPs retained structural integrity over a broad Fe input range up to 27.5 mg. Qualitative comparison of the STEM images indicated that higher CSNP inputs were accompanied by a greater apparent CSNP content within the nanospheres and smaller SMART RHESIN diameters. In contrast, synomag-D showed a qualitative encapsulation threshold: well-defined nanospheres were obtained up to approximately 2.5 mg Fe, whereas higher Fe inputs caused excess non-encapsulated CSNPs. Cubic CSNPs were encapsulated within the nanospheres, but the filling density and morphology strongly depended on core size. Overall, Series 3 shows that CSNP input concentration directly affects the qualitative filling density, but the resulting nanosphere size, shell thickness and uniformity are governed by CSNP coating, size, and morphology.

Series 4 investigated whether two different NP types can be co-encapsulated within SMART RHESINs under the optimised synthesis conditions using DHB and a 15 min mixing time. Five NP mixtures were tested: synomag-D with cubic iron oxide CSNPs SR39 (SI 1, Fig. S1.6f and Table S1.6, entry 6), PVP-coated luminescent upconverting NPs (UCNPs) with SPA20-10 CSNPs SR40 (SI 1, Fig. S1.6g and Table S1.6, entry 7), PEG-coated luminescent UCNPs with SPA20-10 CSNPs SR41 (SI 1, Fig. S1.6h and Table S1.6, entry 8), PVP-coated UCNPs with synomag-D SR42, and PEG-coated UCNPs with synomag-D SR43 (SI 1 on Series 1–5, Series 4 and SI 5 on UCNPs). Co-encapsulation was neither achieved for synomag-D/cubic CSNPs SR39, where separately filled SMART RHESIN populations were observed (SI 1, Fig. S1.6f and Table S1.6, entry 6), most likely due to the markedly different surface chemistries of the two CSNP types, namely the dextran shell of synomag-D and the PMAO coating of the cubic CSNPs, which may promote their partitioning into distinct micellar environments rather than joint incorporation into the same nanocapsules, nor for PVP-coated UCNP mixtures SR40 and SR42 (SI 1, Fig. S1.6g, i and Table S1.6, entries 7 and 9), where EDXS did not confirm UCNP incorporation into the magnetic SMART RHESINs (SI 1, Fig. S1.7a–d and i–l). In contrast, PEG-coated UCNPs could be co-encapsulated with SPA20-10 CSNPs SR41 and synomag-D SR43 (SI 1, Fig. S1.6h, j and Table S1.6, entries 8 and 10), as confirmed by Fe and F signals in EDXS mappings (SI 1, Fig. S1.7e–h and m–p). However, most nanospheres were still predominantly filled with only one magnetic CSNP type, indicating that NP surface chemistry and concentration balance are critical for efficient co-encapsulation. Series 4 therefore demonstrates formulation-dependent co-encapsulation and defines current compatibility limits rather than establishing a universal co-encapsulation protocol.

Series 5 investigated whether polymer additives can be used to tune SMART RHESIN size and shell thickness under the optimised synthesis conditions. PEG and PVP were added to the micelle-forming solution at low and high concentrations using either SPA20-10 CSNPs SR46, SR47, SR50, and SR51 (SI 1, Fig. S1.8a–e and Table S1.7) or synomag-D SR44, SR45, SR48, and SR49 (SI 1, Fig. S1.8f–j and Table S1.8), with additive-free reference systems SR28 and SR34. For SPA20-10 CSNPs, PEG and low-concentration PVP had only minor effects on particle size and shell thickness, while high PVP compromised the nanosphere structure in SR51. In contrast, synomag-D-based SMART RHESINs were more sensitive to polymer additives. Low PEG SR44 and especially low PVP SR48 reduced the nanosphere diameter and shell thickness compared to additive-free SR34, whereas high PEG SR45 produced larger particles and high PVP SR49 disrupted the structure. Overall, low PVP was the most effective additive for generating smaller synomag-D-loaded SMART RHESINs with thinner shells, while high PVP concentrations were detrimental and PEG was better tolerated.

Taken together, Series 1–5 did not reveal a transferable relationship between individual CSNP properties and SMART RHESIN morphology. The observed effects were specific to each CSNP system and formulation.

MPS studies

The MPI signal originates from the non-linear dynamic magnetisation response of the tracer to an oscillating excitation field and is governed by both Néel and Brownian relaxation mechanisms. This dynamic response is the physically relevant observable for MPI applications and is directly accessed by MPS, whereas static $M(H)$ curves do not contain this dynamic information. MPS is therefore used here as the primary magnetic characterization technique for SMART RHESINs. To further assess the SMART RHESINs, their alternating current (AC) magnetic properties were analysed using MPS (MPS-3, Bruker BioSpin GmbH & Co. KG). MPS is an easy and fast method to predict the suitability of the tracers for MPI. The MPS excitation frequency was 25.25 kHz and excitation amplitude 20 mT. The spectra show both the amplitude and the phase orientation as a function of frequency, where only odd harmonics are plotted (Fig. 4). A large amplitude and a shallow slope drop in the signal is preferred for good image reconstruction. In general, the MPS spectra represents the frequency decomposition of the receive signal where each frequency component is represented by the signal's amplitude and phase.

As previously shown by Feye *et al.*, SMART RHESINs can maintain consistent effective relaxation even when subjected to changes in viscosity.[14,15] Both Brownian and Néel relaxation contribute to this effective relaxation. These findings indicate that if the MPS signal amplitudes and phase orientations of mobile (dispersed in deionised H_2O) and immobilised (dispersed in 10 mg mL^{-1} agar–agar) CSNPs or SMART RHESINs are nearly identical, the MPI image can be accurately reconstructed using the same system function or particle model. This is attributed to the unaltered effective relaxation. All measured spectra are provided in SI 6. It is important to note that some of the MPS data have not been normalized to the individual iron content, as there was insufficient material available for complete sample characterization. Consequently, the y-axis is labelled as $A_k/[\mathrm{A\ m^2}]$, where A_k represents the amplitude of the measured harmonic signal at harmonic k. Due to the large number of measured spectra (SI 6), four representative examples are presented in Fig. 4: NP01 and the encapsulated SR02 (Fig. 4a–d), NP03 and SR33 (Fig. 4e–h), NP04 and SR18 (Fig. 4i–l),

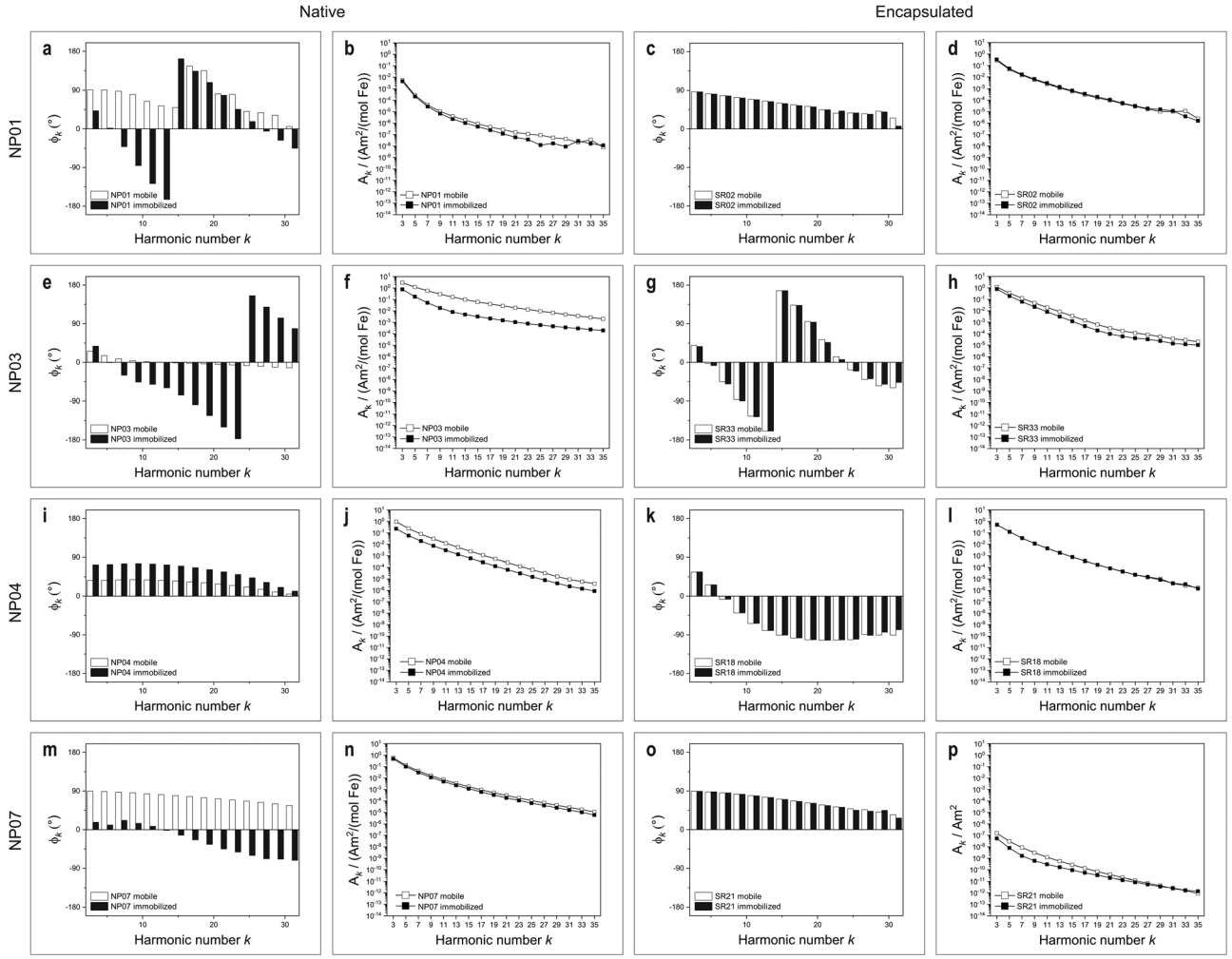


Fig. 4 Selected MPS data of mobile (white bars and rectangular symbols) and immobilised (black bars and rectangular symbols) native and encapsulated CSNPs representing a model system for significant changes in viscosity (water *vs.* agar–agar immobilisation). (a) Phase orientation and (b) amplitude spectra of NP01 (magnetite OH). (c) Phase orientation and (d) amplitude spectra of NP01 encapsulated in SR02. (e) Phase orientation and (f) amplitude spectra of NP03 (synomag-D). (g) Phase orientation and (h) amplitude spectra of NP03 encapsulated in SR33. (i) Phase orientation and (j) amplitude spectra of NP04 (SPA20-10). (k) Phase orientation and (l) amplitude spectra of NP04 encapsulated in SR18. (m) Phase orientation and (n) amplitude spectra of NP07 (cubic iron oxide AKB180PM4). (o) Phase orientation and (p) amplitude spectra of NP07 encapsulated in SR21. For better comparison spectra (b), (d), (f), (h), (j), (l) and (n) have been normalised to the iron concentration of the individual samples. Sample (p) was not normalised due to a shortage of sample material.

and NP07 and SR21 (Fig. 4m–p). MPS data for mobile (white bars and rectangular symbols) and immobilised (black bars and rectangular symbols) native and encapsulated CSNPs were acquired to model significant viscosity changes. Phase orientations and amplitude spectra were analysed to determine the more reliable indicator of unchanged effective relaxation between mobile and immobilised samples (SI 6, Table S6.1). Differences in the $\log_{10}$ amplitude values (ΔA_k) between mobile and immobilised states show slight deviations for native CSNPs and their encapsulated counterparts (Table 1 and Fig. 4b, f, j, n). For NP01, native CSNPs show a mean ± standard deviation (SD) ΔA_k of 0.32 ± 0.21 A m^2 per (mol Fe), while SR02 exhibits a tighter ΔA_k of 0.10 ± 0.10 A m^2 per (mol Fe) (Table 1, entry 1). Similar trends are observed for NP03 and SR33 (ΔA_k = 1.14 ± 0.18 *vs.* 0.39 ± 0.09 A m^2 per (mol Fe), Table 1, entry 2) and NP04 and SR18 (ΔA_k = 0.61 ± 0.01 *vs.* 0.03 ± 0.03 A m^2 per (mol Fe), Table 1, entry 3). In contrast, NP07 shows a reverse trend: native ΔA_k = 0.19 ± 0.05 A m^2 per (mol Fe) *vs.* SR21 ΔA_k = 0.34 ± 0.23 A m^2 per (mol Fe)

Table 1 Differences of the $\log_{10}$ values (Δ) between the mobile and immobilised amplitude A_k [A m^2 per (mol Fe)] data. The data are presented as mean values ± standard deviation (SD). Odd harmonics from k = 3 to k = 35 were considered

		ΔA_k of native CSNPs [A m^2 per (mol Fe)]		ΔA_k of encapsulated CSNPs [A m^2 per (mol Fe)]
Entry	CSNP no.	Mean ± SD	SR no.	Mean ± SD
1	NP01	0.32 ± 0.21	SR02	0.10 ± 0.10
2	NP03	1.14 ± 0.18	SR33	0.39 ± 0.09
3	NP04	0.61 ± 0.01	SR18	0.03 ± 0.03
4	NP07	0.19 ± 0.05	SR21[a]	0.34 ± 0.23

[a] ΔA_k of non-Fe-normalized amplitude data.

This journal is © The Royal Society of Chemistry 2026

(Table 1, entry 4). In the case of NP07, these variations may result from subtle inconsistencies in sample preparation, particularly when working with small volumes. In comparison, phase angle differences ($\Delta\Phi_k$) provide a clearer indication of encapsulation quality. Native CSNPs show notable $\Delta\Phi_k$ shifts upon immobilisation in agar–agar, but encapsulated samples exhibit minimal phase orientation changes. For instance, NP01 $\Delta\Phi_k$ = 76.42 ± 62.84° reduces to 2.62 ± 4.56° in SR02, and similar reductions occur for NP03, NP04, and NP07 encapsulated samples (Table 2, entries 1–4). These observations suggest that phase orientation may provide a more sensitive qualitative indicator than amplitude spectra for assessing deviations in effective relaxation. The data indicate that encapsulating CSNPs in SMART RHESINs results in nearly identical phase orientations for mobile and immobilised samples. This suggests that effective relaxation remains largely unchanged and that the viscosity of the surrounding solution has minimal influence on the signals. Therefore, SMART RHESINs encapsulating CSNPs are well-suited for artefact-free MPI applications under varying microenvironmental conditions. Since synomag-D is one of the NP systems currently regarded as most suitable for MPI, we selected SR33 for MPI measurements due to its strong signal amplitude, including high intensities at higher harmonics. The corresponding results have recently been published.[15] Briefly, we demonstrated that SMART RHESINs, composed of hollow phenolic resin nanospheres encapsulating synomag-D NPs, preserve the magnetic relaxation behaviour of the tracer under varying viscosity conditions. In contrast to unencapsulated synomag-D, where the system matrix acquired in aqueous solution failed to reconstruct the immobilised sample due to viscosity-induced relaxation changes, SMART RHESINs enabled accurate image reconstruction in both mobile and immobilised states using the same aqueous-based system matrix. Phase-angle analysis by MPS therefore provides a rapid qualitative readout for identifying formulations whose effective relaxation is less affected by immobilisation. This encapsulation approach supports robust MPI reconstruction under strongly different microenvironmental conditions and provides a basis for future multifunctional tracer development. Overall, the selected representative SMART RHESINs showed substantially smaller mobile–immobilised phase deviations than their corresponding native CSNPs. These MPS data support the use of phase orientation as a qualitative screening readout for identifying formulations with stable effective relaxation. MPI reconstruction was then used to test this behaviour in spatially resolved phantom experiments.

Table 2 Differences of the values of the mobile and immobilised phase Φ_k [°] data. The data are presented as mean values ± standard deviation (SD). Odd harmonics from k = 3 to k = 35 were considered

Entry	CSNP No.	$\Delta\Phi_k$ of native CSNPs [°] Mean ± SD	SR No.	$\Delta\Phi_k$ of encapsulated CSNPs [°] Mean ± SD
1	NP01	76.42 ± 62.84	SR02	2.62 ± 4.56
2	NP03	86.00 ± 48.03	SR33	4.10 ± 3.26
3	NP04	25.79 ± 12.11	SR18	4.26 ± 10.23
4	NP07	103.33 ± 23.83	SR21	3.81 ± 7.24

MPI studies

While MPS provides valuable insights into the fundamental magnetic behaviour of NPs, MPI enables their spatially resolved visualisation. Central to this imaging modality is the system matrix (SM), which is acquired experimentally using a defined physical calibration sample. The SM quantitatively describes the spatial encoding process by mapping the NP response at each calibration position to the corresponding detector signal. Image reconstruction critically relies on the validity of this mapping. If the physicochemical environment of the NPs changes, for example when they are dispersed in water compared to being immobilised in agar–agar, their relaxation dynamics may be altered and the calibration may no longer accurately reflect the measured signal.[15] Such a mismatch can introduce systematic errors or artefacts into the reconstructed images when only a single calibration is used. However, if environment-dependent signal changes are characterised using separate system matrices, they can also provide additional contrast and be detected by multi-colour MPI. Roeper *et al.* illustrated this application-specific use with a SPION-containing liquid embolic agent, whose magnetic response changed during solidification and could therefore be exploited to monitor the curing process by multi-contrast MPI.[50]

To investigate reconstruction robustness under varying microenvironmental conditions, we considered two reconstruction strategies. In the single system matrix approach, reconstructions rely on a calibration acquired with NPs in water. While straightforward, this method is prone to inaccuracies when particle dynamics differ in immobilised states. The multi-colour approach, in contrast, incorporates SMs obtained under distinct conditions, in this case SR29 dispersed in both water and agar–agar, and concatenates them prior to reconstruction. This enables the separation of contributions from different microenvironments into distinct image channels, although minor signal leakage between channels may occur due to correlations within the combined calibration data. In the present study, emulated two-compartment phantoms containing one virtual sample in water and one in agar–agar were employed to provide a controlled framework for comparing both reconstruction strategies. SR29 was selected for MPI phantom experiments to determine whether the reconstruction robustness previously demonstrated for SR33, which contains dextran-coated, nanoflower-like synomag-D particles,[15] extends to a formulation based on single-core, PMAO-coated CSNPs. The SPA20-10 particles used for SR29 were particularly suitable for this purpose because their PMAO coating showed high compatibility with the SMART RHESIN encapsulation chemistry, yielding structurally intact and sufficiently loaded nanocapsules. Thus, the NP04/SR29 pair provided an appropriate second particle system to investigate, using the multi-colour MPI approach, whether the encapsulation-mediated stabilisation of MPI-relevant relaxation behaviour also applies beyond the synomag-D system. For this comparison, emulated two-compartment

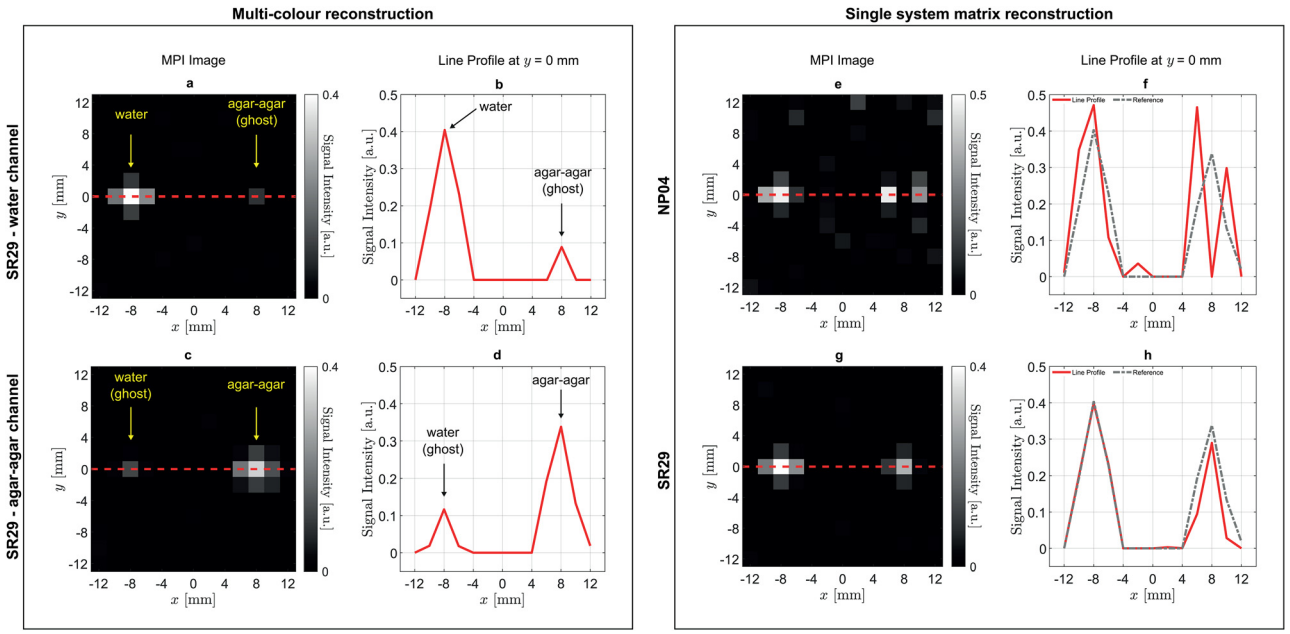


Fig. 5 MPI images (a)–(d) reconstructed using the multi-colour approach with concatenated system matrices from SR29 in water and agar–agar. (a) Reconstruction in the water channel (top row) and (c) reconstruction in the agar–agar channel (bottom row), along with the corresponding line profiles (b) and (d), respectively. This method enables distinct visualisation of the concentration of SR29 in different microenvironments, with only minor ghosting artefacts. MPI images (e)–(h) reconstructed using a single system matrix acquired with NPs in water: (e) NP04 and (g) SR29. (f) and (h) show line profiles along the y = 0 axis for (e) and (g), respectively, including reference concentrations from the multi-colour approach (grey dashed lines). The image with NP04 in (e) reveals significant artefacts due to the system matrix-sample mismatch, as highlighted in (f). The images and corresponding line profiles have a spatial resolution of 2 mm.

phantoms containing one virtual sample in water and one in agar–agar were used to evaluate single- and multi-matrix reconstruction strategies. The results of these reconstruction strategies are illustrated in Fig. 5. Panels a–d show MPI images reconstructed using the multi-colour approach, where the system matrices acquired with SMART RHESINs in both water and agar–agar were concatenated prior to reconstruction. This method enables simultaneous reconstruction of multiple images, each representing the concentrations of the NPs in distinct microenvironments. Fig. 5a and c correspond to SR29 in water and agar–agar, respectively. Minor ghosting artefacts (signal leakage from one reconstruction channel into another), appearing as spurious replicas of structures in the opposite channel (image) due to correlations between the concatenated system matrices, were present but did not compromise the interpretability of the reconstructed images. Fig. 5e–h presents MPI images reconstructed using the single system matrix approach, where NP04 and SR29 were each reconstructed with their respective system matrix acquired in aqueous dispersion. Reconstructions were performed for both SMART RHESINs (encapsulated NP04s) and native NP04s. In each experiment, the emulated phantom contained two samples: one in water at $(x,y) = (-8,0)$ mm and one in agar agar at $(x,y) = (8,0)$ mm. As shown in Fig. 5e, the image corresponding to NP04 exhibits pronounced artefacts, particularly at the location of NPs in agar–agar. This is further illustrated in the line profile in Fig. 5f, which reveals signal distortion and amplitude inconsistencies with respect to the reference concentration estimated using the multi-colour images (dashed grey line) from Fig. 5a–d. These artefacts are attributed to the mismatch between the system matrix acquired with NPs dispersed in water and the signal characteristics of NPs embedded in agar–agar.

In summary, our results show that multi-colour reconstruction can disentangle particle signals originating from different microenvironments, but requires prior knowledge of the respective particle environments. By contrast, SR29 allowed reliable image reconstruction with a single water-acquired system matrix in both mobile and immobilised phantom states. This eliminates the need to anticipate all possible microenvironments in advance and makes SMART RHESINs a more robust and versatile tracer platform for quantitative MPI, particularly in complex biological systems where NP interactions can be difficult to predict.

Preliminary biocompatibility assessment of the empty SR52

As shown in the previous reactions, the CSNP shell occasionally has an influence on the structure of the resulting hollow nanospheres. Therefore, a control reaction was carried out without encapsulating CSNPs to assess the native morphology of the hollow nanospheres in the absence of additional CSNP-related effects. The reaction proceeded under optimied conditions (DHB and 15 min mixing time) as expected and resulted in hollow nanospheres with a clearly visible void space with an HDD of (189.6 ± 20.8) nm and a PDI of 0.042 ± 0.027. The STEM measurements resulted in a d_{SR} of (187.7 ± 21.6) nm for the hollow nanospheres and d_{Shell} of (36.5 ± 5.4) nm (Fig. 6b). From this control reaction, it can be concluded, that the

 This journal is © The Royal Society of Chemistry 2026

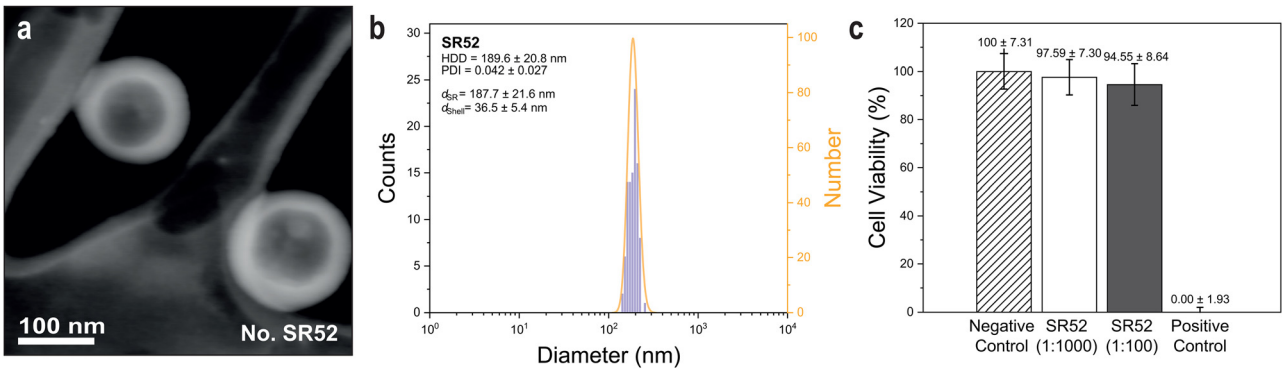


Fig. 6 (a) STEM image of empty hollow nanospheres synthesised under optimised reaction conditions (phenolic monomer DHB, 15 min mixing time). (b) Size distributions obtained by DLS (log-normal number-weighted distribution, HDD and PDI in yellow) and STEM measurements (d_{SR} and d_{Shell}; histogram, n = 100). (c) MTT assay results after incubating HeLa cells with 0.1% and 1.0% dilutions of SR52 corresponding to 1 : 1000 and 1 : 100 dilutions, respectively, in DMEM for 72 hours, followed by MTT treatment, indicating that the empty SR52 hollow nanospheres did not measurably reduce metabolic activity under the tested conditions in comparison with the negative control (without the addition of compound) and the positive control (without metabolic activity). The mean values of n = 8 independent experiments ± standard deviations are shown.

encapsulation, and potentially also the CSNP coating, can influence the micelle forming system and the subsequent formation of hollow nanospheres. This empty SMART RHESIN sample SR52 was therefore used for a preliminary biocompatibility assessment to isolate the contribution of the PFR shell and nanosphere structure from effects caused by encapsulated CSNPs. Accordingly, SR52 (Fig. 6a) was evaluated in wild type HeLa cells as an exploratory material-compatibility screen using the MTT assay (Fig. 6c), which measures metabolic activity based on the reduction of 3-(4,5-dimethylthiazol-2-yl)-2,5-diphenyl-2*H*-tetrazolium bromide (MTT), a yellow tetrazolium salt, by metabolically active cells, to its insoluble formazan with a purple colour. After dissolving the formed formazan, the absorbance of the coloured solution can be measured photometrically at λ = 570 nm using a plate reader. In this experiment, HeLa cells were incubated with 0.1% and 1.0% dilutions of SR52, corresponding to 1 : 1000 and 1 : 100 dilutions, respectively, (with a stock solution mass concentration of 3.6 ± 0.3 mg mL^{-1}) for 72 hours, after which metabolic activity was measured. Generally, substances are considered biocompatible if they reach at least 80% cell viability.[51,52] SR52 showed 97.59 ± 7.30% metabolic activity at 0.1% (dilution of 1 : 1000) and 94.55 ± 8.64% at 1.0% (dilution of 1 : 100), indicating no measurable reduction in HeLa cell metabolic activity under the tested conditions. This observation is limited to the single MTT endpoint and the empty SR52 formulation. It does not establish biocompatibility or haemocompatibility and cannot be extrapolated to CSNP-loaded or surface-modified SMART RHESINs. However, this assay should be interpreted as a preliminary biocompatibility assessment rather than a comprehensive toxicological characterization. For NP-based materials, MTT assays can be affected by optical interference at 570 nm or by adsorption of assay components to the particle surface. Because SR52 consists of empty hollow nanospheres, iron-related redox interference is not expected for this material control, but may become relevant for CSNP-loaded SMART RHESIN formulations.

The present assessment was performed only on SR52 as a representative PFR-shell control. CSNP-loaded formulations, including the SR03-derived material used for PET-CT experiments, were not separately evaluated in this exploratory study. Long-term effects, cell-type-dependent responses, uptake-related effects and inflammatory or oxidative-stress pathways therefore remain to be investigated in future studies. Nevertheless, the preserved metabolic activity observed for SR52 supports the suitability of the PFR shell as a preliminary material platform for further biomedical evaluation.

Surface functionalisation of SMART RHESINs and PET-CT *in vivo* studies

SR03, previously identified for its favourable synthetic characteristics (Series 1), was chosen for further surface modification with ^{18}F for PET-CT imaging. The carboxylic acid group-containing surface of SR03 was covalently functionalised with Eu(III) complex-containing luminescent, amino-functionalised silica NPs, as previously described by Feye *et al.*[14] The aim of the next step was to investigate the biodistribution of the native, non-targeted SMART RHESINs *in vivo*. For this purpose, the amino-functionalised, luminescent SMART RHESINs were further functionalised on the surface with 2,3,4,6-tetrafluorophenyl 6-[^{18}F]fluoronicotinate ([^{18}F]F-Py-TFP) as described in the SI 7 on Methods, section 1.5.[53] This multistep surface modification substantially changes the outer particle interface compared with non-surface-modified SMART RHESINs. The colloidal behaviour observed for the resulting radiolabelled formulation therefore cannot be directly transferred to the non-surface-modified nanocapsules. Fluorine 18 (^{18}F) is a popular and widely used radioisotope due to its optimal physical properties and a half-life of 109.8 minutes.[54,55] All experiments were conducted in accordance with the relevant animal welfare regulations and as approved by the authorities (Regierungspräsidium Tübingen, R 6/19 A, for detailed information, please refer to SI 7, Section 1.5). Male C57BL/6 mice (n = 3) were injected with 10.22 ± 0.46 MBq of the ^{18}F-labelled SMART

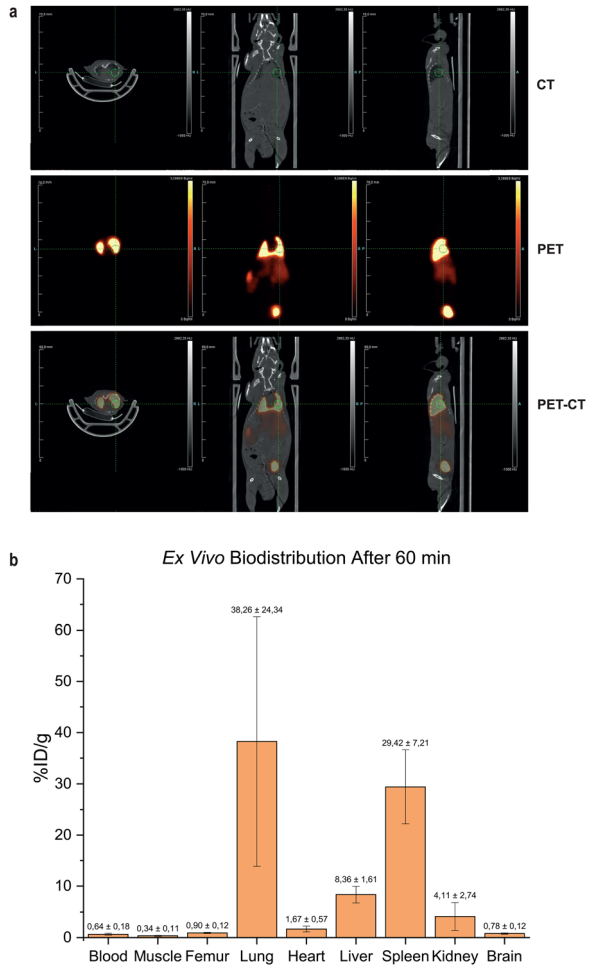


Fig. 7 (a) PET and CT images of a healthy mouse treated with ^{18}F-labelled SMART RHESINs, 50–60 minutes after injection (frame of 10 minutes). (b) *Ex vivo* distribution of ^{18}F-labelled SMART RHESINs 60 min after intravenous administration in mice. The mean values of n = 3 mice ± standard deviations are shown.

RHESINs *via* the tail vein. In order to gain insight into the distribution of the radiotracer within the first hour, one mouse from the group was examined in more detail using a PET scan. The PET/CT images showed a high uptake of ^{18}F-labelled SMART RHESINs in the lungs, possibly due to uptake in the small lung capillaries, and bladder (Fig. 7a). Following the PET and CT scans, the mice were euthanised and all relevant organs were removed for analysis of biodistribution by gamma counter measurement. The data were then presented as injected dose per gram of tissue (ID per g) (Fig. 7b). Consistent with the PET data, the ^{18}F-labelled SMART RHESINs show similar levels of accumulation in the lungs (38.3 ± 29.8% ID per g) and spleen (29.4 ± 8.8% ID per g) and moderate accumulation in the liver (8.4 ± 2.0% ID per g) and kidneys (4.1 ± 3.4% ID per g). The *ex vivo* data provide a first snapshot of organ distribution 60 min after injection. It was also observed during preparation that the ^{18}F-labelled SMART RHESINs tended to aggregate in combination with the injection solution. Although the sample was vortexed again before injection, the particles quickly settled. This makes it particularly difficult to inject equal amounts of activity. This likely contributed to the high variability observed for lung accumulation (38.3 ± 29.8% ID per g). For subsequent experiments, the stability of the ^{18}F-labelled SMART RHESINs in different buffer solutions must therefore first be investigated.

Experimental

Detailed experimental procedures, reagent sources, equipment, NP syntheses, SMART RHESIN syntheses, and analytical methods are provided in the SI. Briefly, SMART RHESINs were synthesised by soft-templated polycondensation using mixed P123/sodium oleate micelles as the structure-directing system.[14] Magnetic CSNPs were introduced into the micellar dispersion and encapsulated during phenolic formaldehyde resin shell formation from phenolic monomers and hexamethylenetetramine. The design space was explored by varying the phenolic monomer, CSNP shell chemistry, CSNP concentration and micelle-forming additive. Particle size and morphology were analysed by DLS and STEM, including hydrodynamic diameter, polydispersity index, SMART RHESIN diameter and shell thickness. Magnetic properties were evaluated by MPS under mobile and immobilised conditions. Selected formulations were further assessed by MPI, radiolabelling and PET-CT, and the control sample SR52 was evaluated in a preliminary MTT-based biocompatibility assay.

Conclusions

This work establishes SMART RHESINs as a versatile nanocapsule platform that translates a broad range of magnetic NP into a common, chemically addressable architecture. Across 52 reactions, ten distinct magnetic CSNP types were tested, including lab-synthesised magnetite (polar and oleic-acid-coated variants), synomag-D, Ocean NanoTech particles (SPA20-10, SOR20-10, SMG20-05), cubic iron oxide NPs (AKB180PM4 and AKB121PM4), and biogenic magnetosomes (wild-type and Δ*feoAB1*, with aggregation in the reaction medium limiting encapsulation efficiency). The co-encapsulation of luminescent UCNPs with two different magnetic CSNP systems expanded the platform, while the unsuccessful combinations identified formulation-specific compatibility limits. Together, these results define the formulation scope and compatibility limits of the current synthesis. Polar and polymer-stabilised CSNPs were generally more compatible, but particle size, surface coating, concentration, and micelle composition did not have consistent effects across the investigated CSNP systems. The screening therefore does not establish a predictive relationship between CSNP properties and the morphology or magnetic response of the resulting nanocapsules. Functionally, MPS indicates reduced viscosity-induced relaxation changes for selected representative SMART RHESIN formulations, and phantom MPI demonstrates multi-colour reconstruction that simultaneously resolves the aqueous and immobilised states of SR29 within a single field of view, a capability that was not achieved with native NP04 under the same reconstruction conditions and is consistent with the

 This journal is © The Royal Society of Chemistry 2026

stabilising role of the SMART RHESIN architecture. Additional functionality was introduced through co-encapsulation of PEG-coated UCNPs and through ^{18}F-radiolabelling of the PFR shell, demonstrated by exploratory PET/CT imaging. Empty SR52 nanospheres preserved HeLa metabolic activity above 94% after 72 h, supporting the suitability of the PFR shell for further biomedical evaluation. Future work will focus on integrating magnetic, optical, therapeutic, and targeting functionalities within single SMART RHESIN architectures, and on systematic toxicological evaluation of CSNP-loaded formulations. Together, these results position SMART RHESINs as a modular platform for building multifunctional magnetic nanocapsules whose architecture can be expanded beyond magnetism by optical, radiochemical and future targeting functionalities.

Author contributions

E. S. R. was responsible for conceptualization, methodology, project administration, formal analysis, and writing – original draft, including the overall project concept, coordination of the study, design of the SMART RHESIN experiments, and interpretation of the results. J. F. contributed to methodology, investigation, and formal analysis by planning and performing the SMART RHESIN syntheses and characterization, MPS and MPI experiments. P. W. R. contributed Resources by providing the analytical infrastructure and enabling the luminescence functionalisation. D. R., J. T., C. F., A. G. R., L. P., and C. R. contributed to investigation and visualisation by acquiring and providing electron microscopy data. F. M., S. T., R. U., and D. S. contributed resources and investigation by preparing magnetosome NPs. A. G. R. and A. L. contributed resources and investigation by preparing cubic NPs. L. P. and C. R. contributed resources and investigation by preparing UCNP NPs. J. F. and S. I. contributed resources, investigation, formal analysis, and visualisation by facilitating MPS and MPI experiments and performing image reconstruction. A. M. contributed resources, investigation, formal analysis and cisualisation by conducting and analysing the PET-CT scans. H.-A. W. and E. L. contributed resources, investigation, and formal analysis by generating and analysing the cytotoxicity data. All authors contributed to writing – review & editing, critically revised the manuscript, and approved the final version.

Conflicts of interest

Jochen Franke and Julia Feye are employees of Bruker BioSpin GmbH & Co. KG. Serhat Ilbey was an employee of Bruker BioSpin GmbH & Co. KG at the time the work was conducted. All other authors declare no conflict of interest.

Data availability

The data supporting this article are included in the article and its supplementary information (SI). Supplementary information: SI 1 contains data for reaction series 1–5, including reaction conditions, particle size data and STEM images structured by series. SI 2 contains the complete set of reaction conditions. SI 3 contains particle-size analysis obtained by DLS and STEM. SI 4 contains additional STEM images of SR01–SR52. SI 5 contains the UCNP characterisation. SI 6 contains MPS amplitude and phase spectra. SI 7 contains experimental methods, including CSNP and SMART RHESIN syntheses. See DOI: https://doi.org/10.1039/d6tc02161a.

Acknowledgements

This work was funded by the Deutsche Forschungsgemeinschaft (DFG, German Research Foundation, 363034336 to E. S. R., INST 91/374-1 LAGG to R. U. and D. S., and SCHU 1080/26-1 to D. S.), supported by the Baden-Württemberg Cooperative State University Karlsruhe Innovation Program Research (IPF) to E. S. R. and a graduate scholarship granted by the State of Baden-Württemberg (Landesgraduiertenförderung to J. F.). Further funding was received from the European Research Council (ERC-2023-PoC, grant ''BacToMagicle'' to D. S.) and the Federal Ministry of Education and Research (BMBF) (grant MagBioFab to R. U. and D. S.). A. L. and A. G. R. acknowledge the financial support of the projects RTI2018-095495-J-I00 and RYC2019-027449-I from the MCIN/AEI/10.13039/501100011033, and the project 2021-SGR-00651 from the Generalitat de Catalunya. The ICN2 is funded by the CERCA programme/Generalitat de Catalunya. The ICN2 is supported by the Severo Ochoa Centres of Excellence programme, Grant CEX2021-001214-S, funded by MCIN/AEI/10.13039.5011000 11033. L. P. and C. R. acknowledge the funding received by ANR (NanoFBI project, PRC ANR-21-CE09-0018). The authors thank Matthias Schlotter (Dept. Microbiology, University of Bayreuth) for expert technical assistance with cultivation of *M. gryphiswaldense* strains and magnetosome isolation.

References

1 Y. A. Koksharov, S. P. Gubin, I. V. Taranov, G. B. Khomutov and Y. V. Gulyaev, *J. Commun. Technol. Electron.*, 2022, **67**, 101–116.
2 C. Chen, J. Ge, Y. Gao, L. Chen, J. Cui, J. Zeng and M. Gao, *Wiley Interdiscip. Rev.: Nanomed. Nanobiotechnol.*, 2022, **14**, 1–22.
3 H. T. K. Duong, A. Abdibastami, L. Gloag, L. Barrera, J. J. Gooding and R. D. Tilley, *Nanoscale*, 2022, **14**, 13890–13914.
4 J. Franke, N. Baxan, H. Lehr, U. Heinen, S. Reinartz, J. Schnorr, M. Heidenreich, F. Kiessling and V. Schulz, *IEEE Trans. Med. Imaging*, 2020, **39**, 4335–4345.
5 S. J. Kemp, R. M. Ferguson, A. P. Khandhar and K. M. Krishnan, *RSC Adv.*, 2016, **6**, 77452–77464.
6 S. J. Kemp, R. M. Ferguson, A. P. Khandhar and K. M. Krishnan, *RSC Adv.*, 2016, **6**, 77452–77464.
7 C. Lu, L. Han, J. Wang, J. Wan, G. Song and J. Rao, *Chem. Soc. Rev.*, 2021, **50**, 8102–8146.

8 K. D. Petrov and A. S. Chubarov, *Encyclopedia*, 2022, **2**, 1811–1828.
9 A. Mittal, I. Roy and S. Gandhi, *Magnetochemistry*, 2022, **8**, 1–32.
10 D. Schüler and M. Köhler, *Zentralbl. Mikrobiol.*, 1992, **147**, 150–151.
11 D. Schultheiss and D. Schüler, *Arch. Microbiol.*, 2003, **179**, 89–94.
12 D. Schüler and F. D. Müller, in *Bacterial Organelles and Organelle-like Inclusions*, ed. D. Jendrossek, Springer International Publishing, Cham, 2020, pp. 53–70.
13 D. Schüler, M. Dziuba, D. Pfeiffer and R. Uebe, *Nat. Rev. Microbiol.*, 2026, **24**, 168–182.
14 J. Feye, J. Matthias, A. Fischer, D. Rudolph, J. Treptow, R. Popescu, J. Franke, A. L. Exarhos, Z. A. Boekelheide, D. Gerthsen, C. Feldmann, P. W. Roesky and E. S. Rösch, *Small*, 2023, **19**, 1–13.
15 J. Feye, J. Franke, J. Treptow, C. Feldmann, P. W. Roesky and E. S. Rösch, *Int. J. Magn. Part. Imaging*, 2025, **11**, 1–5.
16 M. Salimi, W. Wang, S. Roux, G. Laurent, R. Bazzi, P. Goodwill, G. Liu and J. W. M. Bulte, *Nanoscale Adv.*, 2025, **7**, 1018–1029.
17 A. Remmo, D. Eberbeck, O. Kosch, L. Kampen, A. Ludwig, A.-N. Egler-Kemmerer, F. Wiekhorst and N. Loewa, *ACS Appl. Nano Mater.*, 2024, **7**, 24315–24324.
18 B. Gleich and J. Weizenecker, *Nature*, 2005, **435**, 1214–1217.
19 J. Weizenecker, B. Gleich, J. Rahmer, H. Dahnke and J. Borgert, *Phys. Med. Biol.*, 2009, **54**, L1–L10.
20 J. Franke and J. Chacon-Caldera, in *Magnetic Materials and Technologies for Medical Applications*, ed. A. M. Tishin, Woodhead Publishing, 2022, pp. 339–393.
21 K. Lu, P. W. Goodwill, E. U. Saritas, B. Zheng and S. M. Conolly, *IEEE Trans. Med. Imaging*, 2013, **32**, 1565–1575.
22 O. Buchholz, K. Sajjamark, J. Franke, H. Wei, A. Behrends, C. Münkel, C. Grüttner, P. Levan, D. von Elverfeldt, M. Graeser, T. Buzug, S. Bär and U. G. Hofmann, *Theranostics*, 2024, **14**, 324–340.
23 T. E. Torres, E. Lima, Jr., M. P. Calatayud, B. Sanz, A. Ibarra, R. Fernandez-Pacheco, A. Mayoral, C. Marquina, M. R. Ibarra and G. F. Goya, *Sci. Rep.*, 2019, **9**, 3992.
24 P. W. Goodwill, E. U. Saritas, L. R. Croft, T. N. Kim, K. M. Krishnan, D. V. Schaffer and S. M. Conolly, *Adv. Mater.*, 2012, **24**, 3870–3877.
25 J. Rahmer, A. Halkola, B. Gleich, I. Schmale and J. Borgert, *Phys. Med. Biol.*, 2015, **60**, 1775.
26 R. M. Ferguson, A. P. Khandhar, H. Arami, L. Hua, O. Hovorka and K. M. Krishnan, *Biomed. Tech.*, 2013, **58**, 493–507.
27 N. Hoshyar, S. Gray, H. Han and G. Bao, *Nanomedicine*, 2016, **11**, 673–692.
28 M. Kumar, P. Kulkarni, S. Liu, N. Chemuturi and D. K. Shah, *Adv. Drug Delivery Rev.*, 2023, **194**, 114708.
29 J. Wu, *J. Pers. Med.*, 2021, **11**, 771.
30 S. K. Hobbs, W. L. Monsky, F. Yuan, W. G. Roberts, L. Griffith, V. P. Torchilin and R. K. Jain, *PNAS*, 1998, **95**, 4607–4612.
31 F. Alexis, E. Pridgen, L. K. Molnar and O. C. Farokhzad, *Mol. Pharm.*, 2008, **5**, 505–515.
32 Y.-K. Huang, C.-H. Su, J.-J. Chen, C.-T. Chang, Y.-H. Tsai, S.-F. Syu, T.-T. Tseng and C.-S. Yeh, *ACS Appl. Mater. Interfaces*, 2016, **8**, 14470–14480.
33 A. V. S. Lourenço, C. A. Kodaira, E. M. Ramos-Sanchez, M. C. F. C. Felinto, H. Goto, M. Gidlund, O. L. Malta and H. F. Brito, *J. Inorg. Biochem.*, 2013, **123**, 11–17.
34 J. Park, K. An, Y. Hwang, J.-G. Park, H.-J. Noh, J.-Y. Kim, J.-H. Park, N.-M. Hwang and T. Hyeon, *Nat. Mater.*, 2004, **3**, 891–895.
35 J. Liu, S. Z. Qiao, J. S. Chen, X. W. Lou, X. Xing and G. Q. Lu, *Chem. Commun.*, 2011, **47**, 12578–12591.
36 M. Priebe and K. M. Fromm, *Chem. – Eur. J.*, 2015, **21**, 3854–3874.
37 T. Mitsunaga, A. H. Conner and C. G. Hill Jr, *J. Appl. Polym. Sci.*, 2002, **86**, 135–140.
38 A.-H. Lu, W.-C. Li, G.-P. Hao, B. Spliethoff, H.-J. Bongard, B. B. Schaack and F. Schüth, *Angew. Chem., Int. Ed.*, 2010, **49**, 1615–1618.
39 G.-H. Wang, Q. Sun, R. Zhang, W.-C. Li, X.-Q. Zhang and A.-H. Lu, *Chem. Mater.*, 2011, **23**, 4537–4542.
40 P. Carrott, L. Marques and M. R. Carrott, *Microporous Mesoporous Mater.*, 2012, **158**, 170–174.
41 Y. Fang, D. Gu, Y. Zou, Z. Wu, F. Li, R. Che, Y. Deng, B. Tu and D. Zhao, *Angew. Chem., Int. Ed.*, 2010, **49**, 7987–7991.
42 G.-H. Wang, J. Hilgert, F. H. Richter, F. Wang, H.-J. Bongard, B. Spliethoff, C. Weidenthaler and F. Schüth, *Nat. Mater.*, 2014, **13**, 293–300.
43 Q. Sun, C.-Z. Guo, G.-H. Wang, W.-C. Li, H.-J. Bongard and A.-H. Lu, *Chem. – Eur. J.*, 2013, **19**, 6217–6220.
44 Y. Yang, X. Song, Y. Yao, H. Wu, J. Liu, Y. Zhao, M. Tan and Q. Yang, *J. Mater. Chem. B*, 2015, **3**, 4671–4678.
45 S. A. Kulkarni and S.-S. Feng, *Pharm. Res.*, 2013, **30**, 2512–2522.
46 Z. Zhao, A. Ukidve, V. Krishnan and S. Mitragotri, *Adv. Drug Delivery Rev.*, 2019, **143**, 3–21.
47 H. Li, K. Jin, M. Luo, X. Wang, X. Zhu, X. Liu, T. Jiang, Q. Zhang, S. Wang and Z. Pang, *Cells*, 2019, **8**, 881.
48 P. R. Lockman, M. O. Oyewumi, J. M. Koziara, K. E. Roder, R. J. Mumper and D. D. Allen, *J. Controlled Release*, 2003, **93**, 271–282.
49 X. Huang and S. Bhana, U. S. Patent, US 2015/0037818 A1, 2015.
50 F. Roeper, M. Ahlborg, T. Friedrich, A. Malhotra, J. Ackers, E. S. Rösch, M. M. Sieren, M.-J. Buhné, J. Barkhausen, R. Kloeckner, M. Graeser, P. König, T. M. Buzug, K. Lüdtke-Buzug and F. Wegner, *ACS Appl. Nano Mater.*, 2026, **9**(30), 14619–14627.
51 M. Zborowski and J. J. Chalmers, *Magnetic cell separation*, Elsevier, 2011.
52 M. Mahmoudi, A. Simchi, A. S. Milani and P. Stroeve, *J. Colloid Interface Sci.*, 2009, **336**, 510–518.
53 R. A. Davis, C. Drake, R. C. Ippisch, M. Moore and J. L. Sutcliffe, *RSC Adv.*, 2019, **9**, 8638–8649.
54 R. Chakravarty, S. Goel, A. Dash and W. Cai, *Q. J. Nucl. Med. Mol. Imaging*, 2017, **61**, 181–204.
55 L. Cai, S. Lu and V. W. Pike, *Eur. J. Org. Chem.*, 2008, 2853–2873.

 This journal is © The Royal Society of Chemistry 2026